International Journal of Minerals, Metallurgy and Materials
Accepted manuscript, https://doi.org/10.1007/s12613-024-2977-6

Intelligent identification of acoustic emission Kaiser effect points and its application in efficiently acquiring in-situ stress

Zhangwei Chen[1,2)], *Zhixiang Liu*[1,2)], *Jiangzhan Chen*[1,2),✉], *XiBing Li*[1,2)], *and Linqi Huang*[1,2)]

1) School of Resources and Safety Engineering, Central South University, Changsha 410083, China

2) Hunan Key Laboratory of Resources Exploitation and Hazard Control for Deep Metal Mines, Changsha 410083, China

✉Corresponding author: Jiangzhan Chen E-mail: jiangzhanchen@csu.edu.cn

Abstract: Large-scale underground projects require precise in-situ stress information, and the acoustic emission (AE) Kaiser effect method currently provide lower costs and streamlined procedures. In this method, the accuracy and speed of Kaiser point identification are crucial. Thus, the integration of chaos theory and machine learning for the precise and rapid identification of Kaiser points constitutes the objective of the study. The intelligent model of the AE partitioned areas identification was established by phase space reconstruction (PSR), genetic algorithm (GA), and support vector machine (SVM). Then, the plots of model classification results were made to identify Kaiser points. We refer to this method of identifying Kaiser points as "The Partitioning Plot Method based on PSR-GA-SVM" (PPPGS). The PSR-GA-SVM model demonstrated outstanding performance, achieving a 94.37% accuracy rate on the test set, with other evaluation metrics also indicating exceptional performance. The PPPGS identified Kaiser points similar to the tangent-intersection method, with greater accuracy. Furthermore, in the classification model's feature importance score, the fractal dimension extracted by PSR ranked second after accumulated AE counts, confirming its importance and reliability as a classification feature. To validate practicability, the PPPGS were applied to in-situ stress measurement at a phosphate mine in Guizhou Weng'an, China, demonstrating good performance.

Keywords: Acoustic emission (AE); Kaiser effect; Phase space reconstruction (PSR); Support vector machine (SVM); Genetic algorithms (GA); Classification model.

1 Introduction

With the rapid development of the mining industry and the construction of urban underground spaces, there is a growing trend towards large-scale deep underground mining and excavation of deep tunnels [1-7]. To ensure the safety of construction and personnel in the project, it is necessary to determine the in-situ stress information reliably [8-11]. In the measurement of in-situ stress, traditionally employed methods include the stress relief method by overcoring and hydrofracturing method, etc. Although widely used in engineering measurements, traditional methods show certain limitations and drawbacks. These limitations include high costs, time-consuming and labor-intensive procedures, and difficulty conducting measurements in deep underground areas [12]. Therefore, the acoustic emission (AE) Kaiser effect method has been rapidly developed recently. The Kaiser effect refers to the phenomenon in materials undergoing cyclic loading, where a significant amount of AE signals is detected only when stress surpasses the material's previously experienced maximum stress. The moment when the Kaiser effect occurs is called the Kaiser point. The Kaiser effect was first discovered by Joseph Kaiser in 1950 in metal samples [13], followed by Goodman in 1963 in rocks [14].

The most critical part of the AE Kaiser effect method for in-situ stress measurement is the identification of the Kaiser point, and numerous scholars have already proposed various identification methods for the Kaiser point. Boyce et al. [15] first proposed the tangent-intersection method based on AE features. Hayashi et al. [16] concluded that Kaiser point can be obtained by "take-off point" based on AE counts, and Qin et al. [17] also used this method. Villaescusa et al. [18] combined the take-off point method with the specimen's strain to determine the Kaiser point. Yoshikawa et al. [19] proposed a new method to identify the Kaiser point by loading the specimen twice cyclically and observing the difference in the AE events between the first and second cycles. Later, Srinivasan et al. [20] also employed this method to study the Kaiser effect. Bai et al. [21] suggested a Kaiser point identification method based on the slope and tilt angle of the accumulated AE counts curve. The aforementioned methods can identify Kaiser point and have their respective strengths. However, these methods may have some drawbacks, such as the discriminative conditions are relatively subjective or difficult to identify the Kaiser point in the case of more noise.

Chaos refers to a phenomenon in nonlinear dynamical systems whose characteristics include initial value sensitivity, intrinsic randomness, and ergodicity, which show the complexity and unpredictability of system behavior. It has been studied to different degrees by scholars in many fields. Li et al. [22] investigated the law of AE activity of rock mass through chaotic dynamics theory and extracted the nonlinear features of AE activity. Xue et al. [23] relied on chaos theory to study the deformation law of the slope rock mass, obtained the nonlinear features of the deformation of the slope rock mass, and established an accurate prediction model. Cao et al. [24] accurately predicted and diagnosed the agglomeration phenomenon in a fluidized bed by applying chaos analysis to the AE signals. Some researchers have applied chaos theory to the identification of Kaiser effect points. Zhao et al. [25] used the G-P algorithm to calculate the correlation fractal dimension of AE energy, thereby identifying the Kaiser points. Wang et al. [26] demonstrated the chaotic characteristics of Kaiser point signals in sandstone using wavelet packet analysis and phase space reconstruction (PSR).

In addressing non-linear problems, machine learning serves as a potent solution method. Traditional linear methods have limitations when dealing with non-linear problems, while machine learning can better deal with this complexity. Currently, many scholars have accomplished many prediction and classification tasks by integrating chaos theory with machine learning. Sivakumar et al. [27] studied the nonlinear characteristics of river flow using two nonlinear methods, PSR and artificial neural networks, to predict its dynamics. Fei et al. [28] developed a bearing fault diagnosis model with wavelet packet variation, PSR, and support vector machine (SVM). Su et al. [29] used SVM, PSR, and particle swarm optimization to study the structural model of dam deformation and establish a dam deformation prediction model.

In summary, traditional methods for Kaiser point identification have several limitations, and currently, there is a research gap in integrating chaos theory and machine learning for the identification of the Kaiser point. Hence, this research is directed towards the rapid and accurate identification of Kaiser points, thus embarking upon the following works. The AE activity was analyzed and its nonlinear chaotic features were extracted, by PSR. Then, Genetic Algorithms (GA) and SVM were employed to construct an intelligent identification model of the AE partitioned areas by combining chaotic features with AE features. Finally, the Kaiser points were identified based on classification results. Moreover, the PPPGS was applied to practical

engineering.

2 Experimental device and Rock samples

2.1 Sample preparation

The test specimens were taken from the Shandong Gold Mine, China, located at five different depths, including -1000 m, -1200 m, -1400 m, -1600 m, and -1800 m. The core samples from each depth were made into test specimens, 20 mm~25 mm in diameter and with a 2:1 height-to-diameter ratio. Before testing, intact specimens with fewer cracks were chosen from these samples. Diameter and height measurements were taken for each specimen, and they were numbered accordingly based on their depth.

2.2 Test equipment

The rock specimens underwent uniaxial compressive testing using the MTS815 servo material testing machine, while synchronously collecting load and AE data using the PCI-II multi-channel AE system. The AE system has a sampling rate of up to 40 MHz and can record continuous waveforms in real-time. It can record over 20 characteristic parameters, including AE events, energy, amplitude, counts, rise time, etc. The experimental setup is shown in Fig. 1.

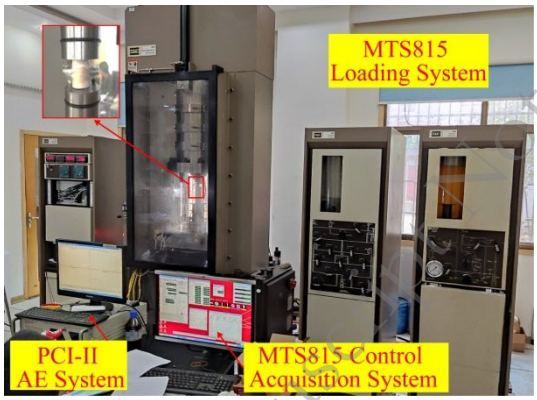

Fig. 1. The experimental setup.

2.3 Loading scheme

The experimental loading method employed displacement-controlled loading at a loading rate of 0.05mm/min. It involved two cycles of loading and unloading, as illustrated in Fig. 2. The AE system's preamplifier is 40 dB, with a sound noise threshold of 40 dB. The AE sensor used has dimensions of Φ 8 mm × 8 mm, resonating at a frequency range of 20~400 kHz, and dual-channel data acquisition is performed at a sampling frequency of 1 MHz. To ensure the regular operation of the sensor, it requires inspection before the experiment. Vaseline was used as a coupling agent between the sensor and the specimen, and both sensors were fixed on opposite sides at the mid-length of the specimen, secured by adhesive tape. To minimize the end effect of the specimen on the experimental results, a layer of Vaseline was uniformly applied to the contact surfaces of both the pressure head and the specimen before the experiment began. Synchronous data acquisition was initiated using the AE system at the start of the experiment.

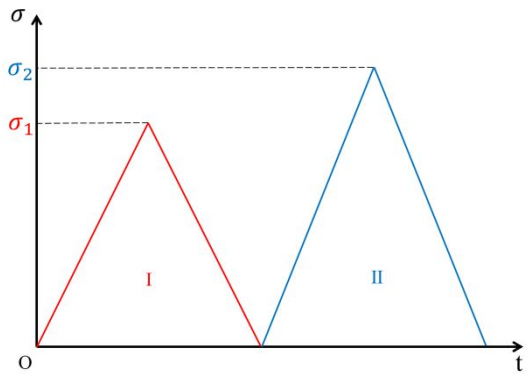

Fig. 2. Loading scheme.

3 Data preprocessing and Feature exploration

3.1 AE data process

After the AE data were obtained experimentally, a curve of accumulated AE counts versus time was made and used for the initial identification of the Kaiser point for each specimen. In the experiments, there were two cycles of loading and unloading, so the specimen underwent the Kaiser effect twice in a single experiment. To identify these two Kaiser points, we utilized the tangent-intersection method, as shown in Fig. 3. In the figure, line A starts from the curve's endpoint and reaches the curve's inflection point, while line B starts from the curve's beginning and reaches the inflection point. The intersection of the two lines corresponds to the time point where the Kaiser point is located. The Kaiser effect points obtained through the tangent-intersection method will be used to validate the applicability of the Kaiser effect to rock samples and will serve as an evaluation criterion in subsequent analyses.

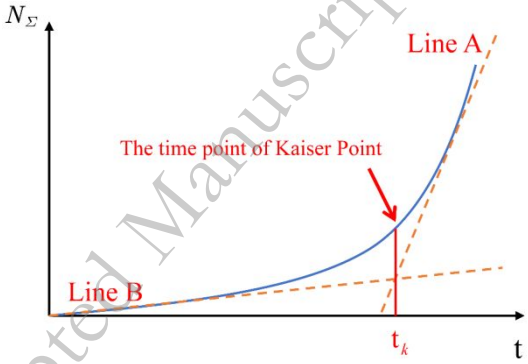

Fig. 3. The tangent-intersection method

3.2 Phase space construction of AE data

Phase space is a useful tool for describing dynamical systems. With the help of a model and an appropriate set of variables, dynamics can represent a real-world system as the geometry of a single moving point.

The time-delay method [30] is one of the most popular methods to reconstruct phase space. This method uses past historical data and an appropriate delay time to reconstruct a scalar (or univariate) time series, where $i = 1, 2, \ldots, N$), representing the underlying dynamics in a multidimensional phase space. The reconstructed phase space can be built as:

$$Y_j = (X_j, X_{j+\tau}, X_{j+2\tau}, \ldots, X_{j+(m-1)\tau}) \tag{3.1}$$

where $j = 1, 2, \ldots, N-(m-1)\tau$, Y_j is the time series, τ is the time delay, and m is the embedding dimension. The parameters m and τ are critical technical parameters for phase space

reconstruction, determining the number of components and the component spacing of the phase points, respectively. Both parameters cannot be chosen arbitrarily. The following describes the parameters to be determined and the obtainable chaotic features for phase space reconstruction.

There are many methods for determining the time delay and embedding dimension[31,32,33]. In this paper, the mutual information method [34] and the false nearest neighbors (FNN) [32] method will be used to determine the time delay and embedding dimension, respectively. The mutual information method offers a quantitative measure of the information shared between the variables, allowing for a more precise selection of the reconstruction parameters. It is appropriate for analyzing complex systems, robust to noise, and capable of handling incomplete information in the phase space reconstruction process [35]. The FNN method was chosen to determine the embedding dimension based on the following idea: If the phase space is reconstructed using a dimension lower than the proper embedding dimension of the system, then the nearest neighbors in the original phase space may be misclassified as non-neighbors in this low-dimensional space, i.e., "false neighbor". The FNN method aims to find these misclassified points and determine the embedding dimensions more suitable for the target system.

The Lyapunov exponent λ is an index used to characterize whether trajectories in phase space are contracting or expanding. When $\lambda < 0$, the trajectory contracts, and the system motion tends to stabilize and is less sensitive to different initial conditions. When $\lambda \geq 0$, the trajectory separates rapidly, making the system susceptible to the initial conditions. In an m-dimensional discrete system, there are usually m Lyapunov exponents $\lambda_i (i = 1, 2, ..., m)$, and if the largest is $\lambda_{\max} \geq 0$, then the system is likely to exhibit chaotic behavior [36]. The Wolf method [37] was used to determine the maximum Lyapunov exponent in this study.

The fractal dimension reflects the geometric structure and distribution characteristics of trajectories in phase space, which can be computed using the G-P algorithm [31]. In previous studies, the G-P algorithm was commonly utilized to calculate the correlation dimension of a univariate time series, eventually deriving the fractal dimension of the time series. In this study, the G-P algorithm was improved to reveal the characteristics of the fractal dimension over time effectively.

The AE features of the specimens, including AE counts, amplitude, and energy, are all univariate time series. Among them, since the AE count can better express the characteristics of the AE data than other parameters and was often used to characterize the AE activity in previous research, the phase space reconstruction of the AE counts was carried out in this study to extract the chaotic features of the AE data.

The AE counts during the uniaxial compression experiments were extracted as a time series for each specimen. Subsequently, for each specimen, estimations were made for delay time and embedding dimension, and then phase space reconstruction was separately conducted. The following outlines the steps of phase space reconstruction for some specimens.

Fig. 4 shows the use of the mutual information method to estimate the delay time of the AE counts time series of rock specimens. The four curves are the time delay curves of four specimens. The mutual information method estimates the entropy of mutual information in the time series at different time delays. It identifies the time delay corresponding to the first local minimum of mutual information entropy and regards it as the optimal time delay of the time series.

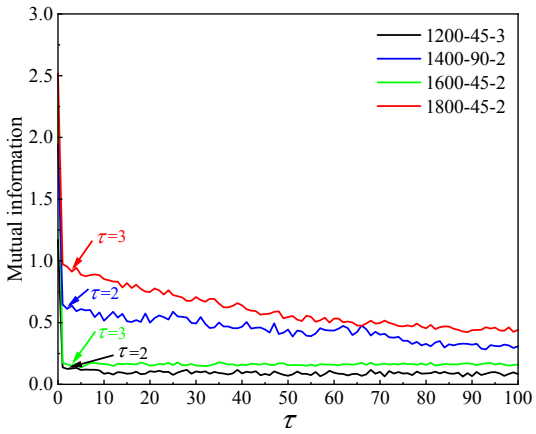

Fig. 4. The time delay estimation via the mutual information method.

Fig. 5 shows the use of the FNN method to estimate the embedding dimension of the AE counts time series. Using Fig. 5(a) as an example, when the embedding dimension is 6, Criterion 1 stabilizes, Criterion 2 keeps increasing, and the joint criterion shows that the false nearest neighbors percentage starts to change from a decreasing to an increasing trend. So, the optimal embedding dimension for this example is 6.

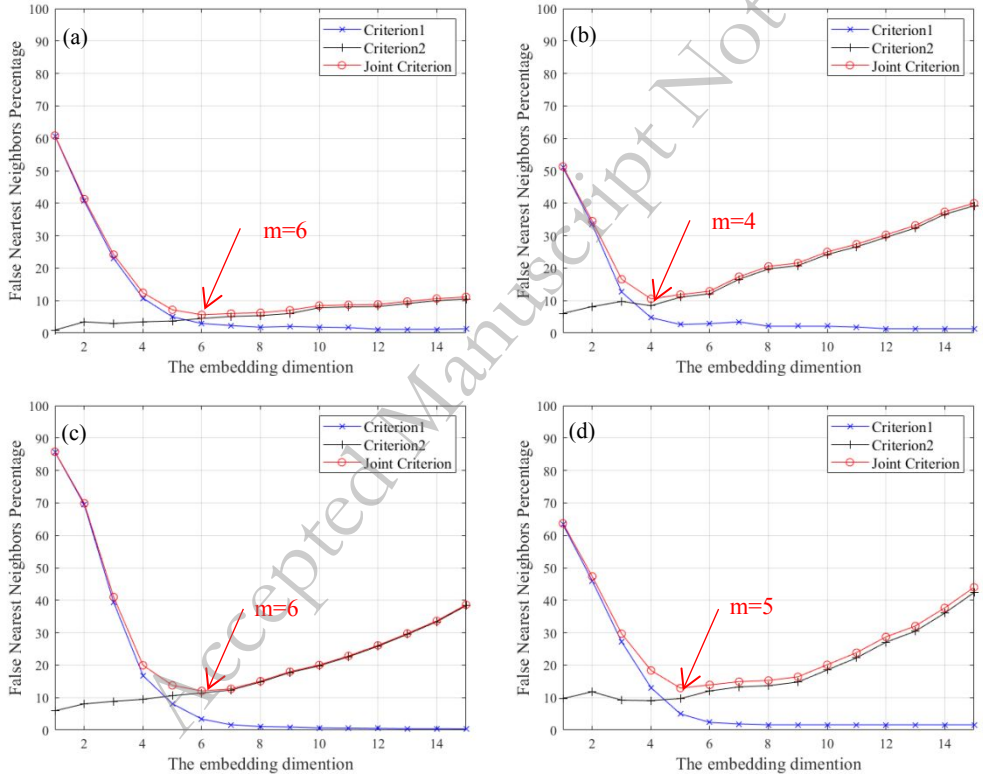

Fig. 5. (a) 1200-45-3. (b) 1400-90-2. (c) 1600-45-2. (d) 1800-45-3. The embedding dimension estimation via FNN method.

Once the time delay and embedding dimension are estimated, the Lyapunov exponent and fractal dimension can be estimated. The Wolf method was used to estimate the Lyapunov exponent, and the estimated values were given in Table 1. As can be seen from Table 1, the Lyapunov exponents of the AE counts time series of the four specimens are all greater than zero.

Table 1. Lyapunov exponent of AE counts time series for four specimens

Specimen number	1200-45-3	1400-90-2	1600-45-2	1800-45-3
Lyapunov exponent	0.4131	0.6786	0.5724	0.7800

The fractal dimension was estimated for each time point in the time series using the improved G-P algorithm, and the curve of fractal dimension over time was shown in Fig. 6. As can be seen from the figure, there is a close relationship between the fractal dimension and the AE counts. The fractal dimension shows a general trend of rising with the increase of the AE counts, interspersed with some cases of decreasing. In other words, as the AE counts increase, the fractal dimension demonstrates an overall upward trend with varying degrees of fluctuations, portraying a phenomenon that is neither entirely random nor regular. Then, combined with the Lyapunov exponent, it fully illustrated that the AE counts have chaotic properties.

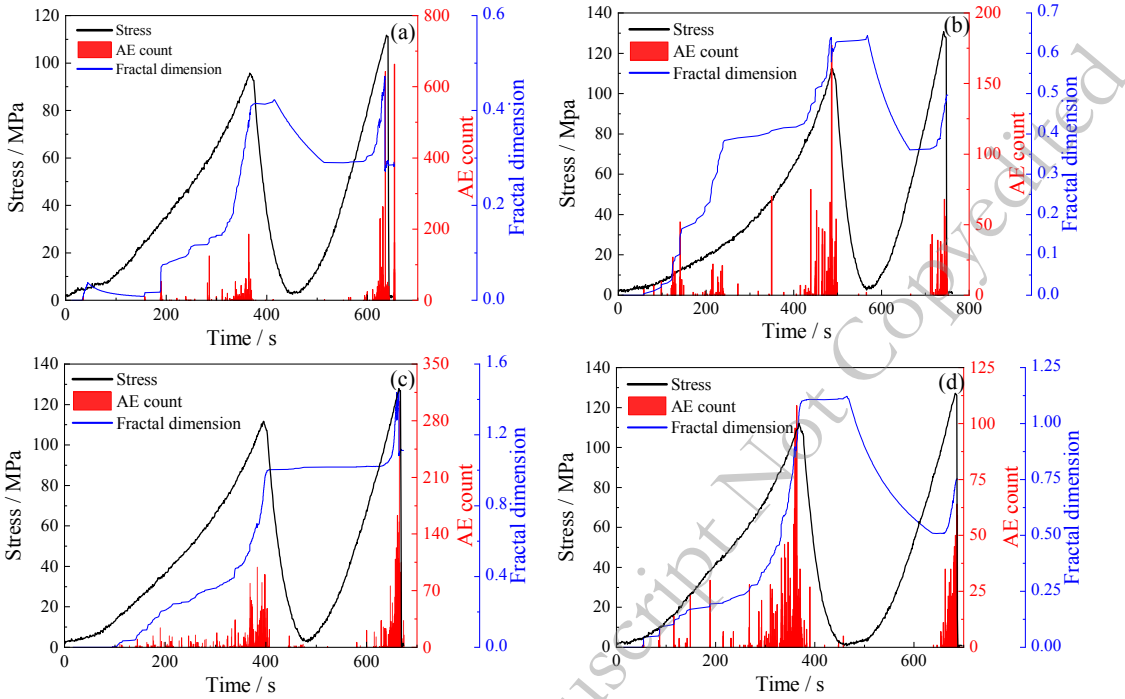

Fig. 6. (a) 1200-45-3. (b) 1400-90-2. (c) 1600-45-2. (d) 1800-45-3. The fractal dimension curve estimation via improved G-P algorithm.

3.3 Preprocessing of SVM datasets

It has been demonstrated in numerous studies [19, 38] that friction-type AE signals caused by the closure of existing fractures and inter-particle friction occur during the early stages of rock loading. These AE signals differ from the fracture-type AE signals caused by the expansion of new fractures used to identify the Kaiser effect. Thus, the two types of AE signals need to be differentiated.

When subjected to uniaxial cyclic loading and unloading, rocks exhibit distinct stages in their stress-time curves, as depicted in Fig. 7. The O(O')A segment represents the compaction stage associated with pore and crack closure. The AB segment represents the elastic deformation stage. It was found in the experiment that friction-type AE occurs in both sections, with less activity in the O(O')A segment and more in the AB segment. So, we set the AB segment of the stress-time curve as "Pore compacting area". In the region, AE signals are friction-type. AE signals activated after point B and before the Kaiser point are considered to exhibit the Felicity effect [39]. This phenomenon is characterized by a significant increase in acoustic emission when the load is less than the highest stress level experienced in the early stages of the cyclic loading process. Therefore, we set this region as "Felicity area". AE signals activated from the Kaiser point up to the point of peak stress can be considered to exhibit the Kaiser effect. So, we set this region as the "Kaiser area". In summary, the AE signals were classified into three areas based on the rock

stress-time curve and the AE data: Pore compacting area, Felicity area, and Kaiser area.

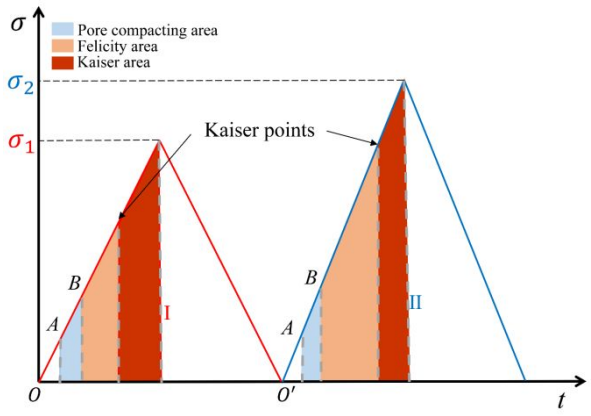

Fig. 7. Stress-time curves of the rocks and the partitioning of the AE signals.

After the experiments, the 60 specimens' AE data were obtained. Then, we employed counts, accumulated counts, energies, and estimated fractal dimensions as features input into the SVM. To mitigate the influence of the data unit on the classification of the SVM model, we applied Min-Max Scaling (Eq.**Error! Reference source not found.**) to normalize the data for each specimen.

$$X_{scale} = \frac{X - X_{\min}}{X_{\max} - X_{\min}} \tag{3.2}$$

In Eq.**Error! Reference source not found.**, X is the original data, $X_{\min}$ is the minimum value of the data, $X_{\max}$ is the maximum value of the data, and X_{scaled} is in the range [0,1].

After normalizing the AE data of 60 specimens, we integrated them into one dataset. However, in the final dataset, we observed that the classified data of the three partitions showed a noticeable imbalance. The proportion of data in Kaiser area was higher than in Pore compacting and Felicity areas. The distribution of the original data is shown in Fig. 8. A dataset with a noticeable imbalance tends to result in poorer classification performance, leading to a decline in the classifier's performance [40]. Therefore, the SMOTETomek [41] method was utilized to process the unbalanced dataset, obtaining a balanced dataset for improving the classifier's performance.

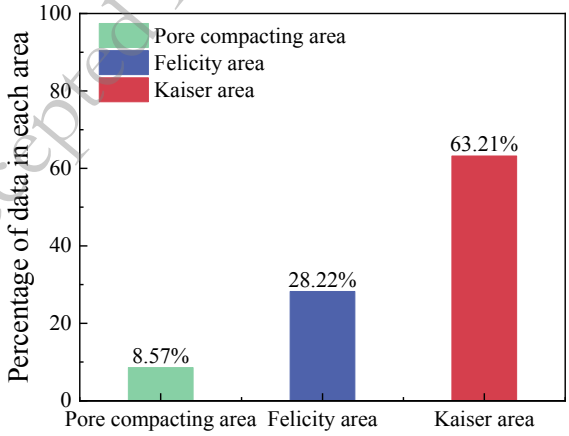

Fig. 8. The Percentage of data in each area in the original dataset.

The dataset processed by the SMOTETomek method contains 100,000 samples (each AE count was considered a sample). The dataset underwent a partition, with 70% allocated to the training set and 30% to the test set. The SVM classification model was constructed using the training set. The Pore compacting area, Felicity area, and Kaiser area were replaced by 1, 2, and 3,

respectively. Each input and output parameter of the model is demonstrated in Table 2.

Fig. 9 depicts the study's flowchart. In the flowchart, Min-Max Scaling and SMOTETomek are used to obtain a balanced normalized dataset. The training set is used to train the SVM model, the GA is used to optimize the hyperparameters of the SVM, and the test set is used to evaluate the model's performance. Finally, the SVM model's classification results are used for Kaiser point identification.

Table 2. Inputs and outputs of the SVM model

Name	Content
Training set	70%× dataset
Test set	30%× dataset
Features	Counts, Accumulated counts, Energy, Fractal dimension
Labels	Pore compacting area, Felicity area, Kaiser area

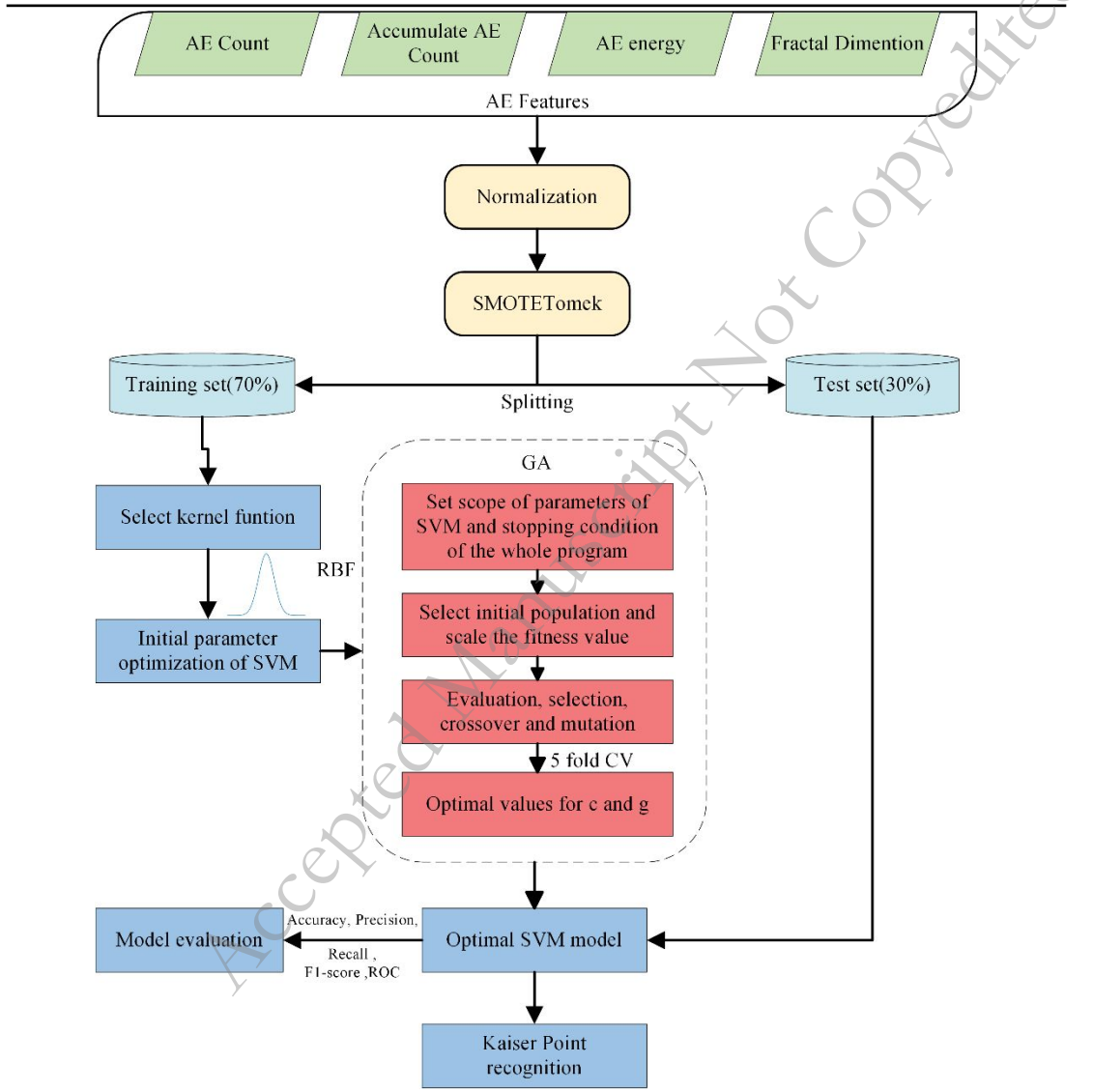

Fig. 9. Flowchart of research.

4 Results and Application

4.1 Model evaluate metrics

In this study, the evaluation metrics chosen for the SVM model were accuracy, precision, recall, and F_1, computed based on the confusion matrix. In addition to these metrics, the receiver operating characteristic curve (ROC) was also used to evaluate the performance of the SVM classifier. Although ROC characteristic curves are often widely used in binary classification

problems, they can also provide helpful information for multiclassification problems.

$$Acc = \frac{TP + TN}{TP + TN + FP + FN} \tag{4.1}$$

$$Precision = \frac{TP}{TP + FP} \tag{4.2}$$

$$Recall = \frac{TP}{TP + FN} \tag{4.3}$$

$$F_1 = \frac{2 \times precision \times recall}{precision + recall} \tag{4.4}$$

4.2 PSR-GA-SVM Parameter setting

The critical parameters to be determined in the SVM model include c and g. The penalty parameter c represents the model's intolerance for errors. The parameter g implicitly determines the data distribution mapped to the new feature space. Therefore, GA was employed to optimize and select parameters c and g. Integrated with five-fold cross-validation, the average accuracy of the model after cross-validation was used as the fitness function. Then, the optimal combination of parameters was sought through multiple iterations of the training set. Fig. 10 displays the procedures to calculate the objective function.

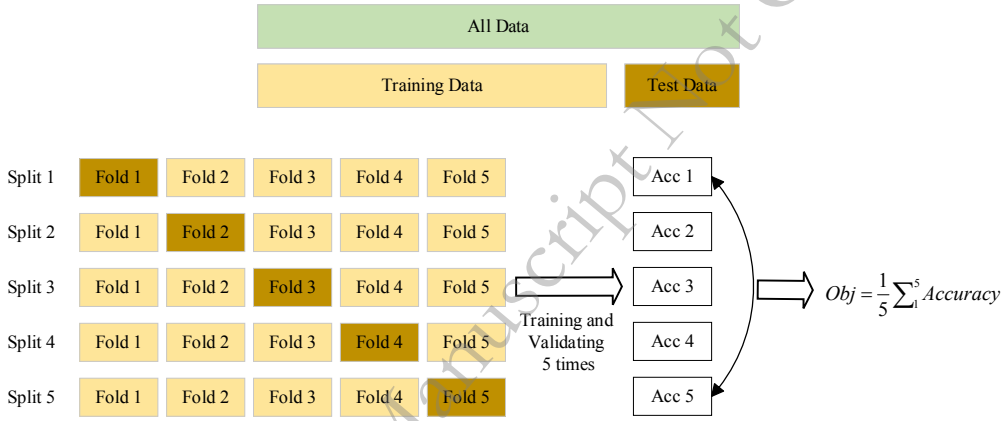

Fig. 10. Flowchart for calculating the objective function.

In the GA, the parameters were configured as follows: 50 genetic iterations, a population size of 20, a crossover probability of 0.7, a mutation probability of 0.02, a cross-validation parameter of 5, and search ranges of [0, 100] for c values and [0, 1000] for g values. Fig. 11 illustrates the iterative convergence process of the fitness function. Throughout 50 iterations, the GA rapidly identified the maximum of the fitness function. The optimized c value was 42.3296, the optimized g value was 349.4727, and the best cross-validation accuracy was 92.76%.

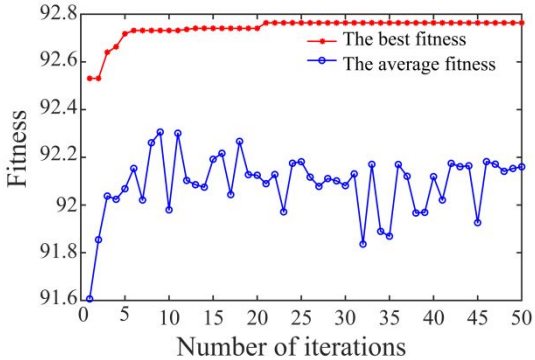

Figure. 11. The iterative convergence of fitness function.

4.3 PSR-GA-SVM classification results and Kaiser point identification

Fig. 12 illustrates the confusion matrix of the test set. Clearly, the model accurately classified the three categories. The individual evaluation metrics based on the confusion matrix are listed in Table 3 and 4. The SVM classification model, built from the training set, exhibited an accuracy of 95.31% during training and 94.37% during testing, demonstrating close similarity. Moreover, the test set accuracy slightly surpassed that of cross-validation. This suggests that the PSR-GA-SVM model avoids overfitting.

The following observations were made based on the model data in Table 4 for the test set. For precision, Pore compacting area and Felicity area were around 90%, and Kaiser area reached 94.58%. Therefore, the model had high precision in predicting all three areas, and performed better in identifying the Kaiser area. For recall, Pore compacting area was as high as 96.08% and Kaiser area also reached 92.84%, which were both higher than 90%, indicating that the model successfully identified more samples from these two areas. In contrast, the recall of Felicity area was only 85.70%. It may be due to the similar features between Pore compacting area and Felicity area, resulting in the model omitting some actual samples in this category and a relatively low recall rate. For F_1, there was not much difference between Pore compacting area and Kaiser area. At the same time, the Felicity area was relatively low but very close to 90%. The above implies that the model achieved a good balance of classification across the three classes and performed relatively well on Pore compacting area and Kaiser area. Overall, these three classes demonstrated excellent precision, recall, and F_1 performance, showcasing the model's outstanding identification capabilities for the three classes.

Fig. 13 illustrates the ROC curves for each class. As observed in the figure, the ROC curves for all three classes are positioned close to the upper-left corner of the plot, indicating higher true positive rates and lower false positive rates. The AUC for each class exceeded 0.95, signifying the excellent classification capabilities of the model for these three classes. A comparison of the AUC of the three categories shows that Kaiser area > Pore compacting area > Felicity area, with a higher AUC indicating better classification ability.

Table 3. Individual evaluation metrics in the training set

Evaluate indexes in the train dataset	Pore compacting area	Felicity area	Kaiser area
Precision	90.97%	91.56%	96.45%
Recall	96.63%	87.68%	94.51%
F_1	93.71%	89.58%	95.47%
Accuracy in the training dataset	95.31%		

Table 4. Individual evaluation metrics in the test set

Evaluate indexes in the test dataset	Pore compacting area	Felicity area	Kaiser area
Precision	90.43%	89.68%	94.58%
Recall	96.08%	85.70%	92.84%
F_1	93.17%	87.65%	93.70%
Accuracy in the test dataset	94.37%		

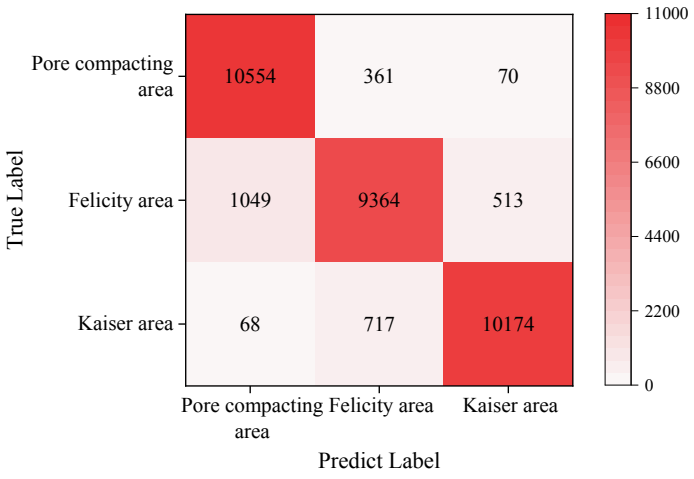

Fig. 12. The confusion matrix for the test set.

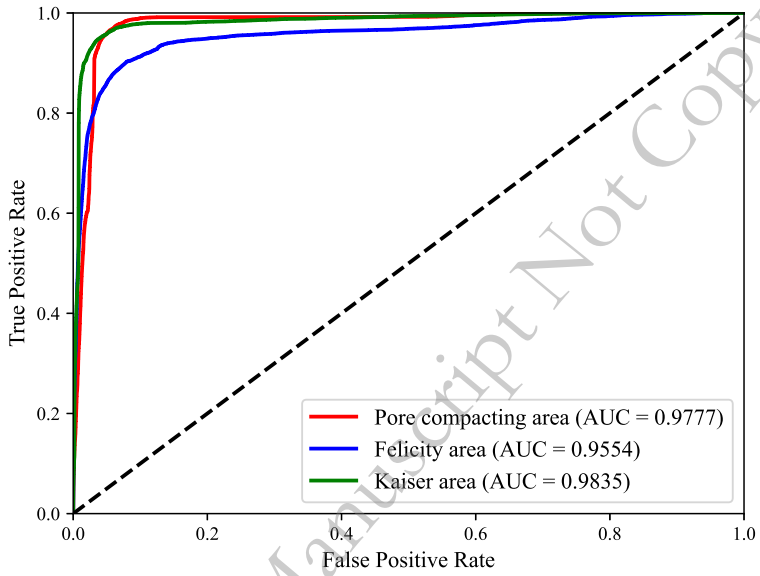

Fig. 13. The ROC curve for the test set.

Fig. 14 shows the partitioning results for the test set, using the 1400-45-3 specimen as an example due to space constraints. The figure's blue, orange, and red scatters show the AE count for the Pore compacting area, Felicity area, and Kaiser area, respectively. Although there were some misclassified results, the overall results were relatively accurate, with clear boundaries observed in each region. Therefore, the point where the classification boundary lines of Felicity area and Kaiser area intersect with the stress-time curves was considered the Kaiser point and we called this method the Partitioning Plot Method base on PSR-GA-SVM model(PPPGS).

In Fig. 14 and 15, the Kaiser points have been marked with green dashed lines, arrows, and circles. Moreover, the corresponding stress values have been provided. Fig. 15 shows two Kaiser points identified by the tangent-intersection method. Observing the two figures, it can be seen that the stresses corresponding to Kaiser point A and Kaiser point B identified by the PPPGS and tangent-intersection method are 85.4 MPa, 94.3 MPa, and 86.2 MPa, 98.3 MPa, respectively. The results of the two methods were very close, showing that the PPPGS accurately identified the Kaiser points. It is worth noting that, due to the peak stress set in the experiment for the first cycle being 95 MPa, the theoretical value of the Kaiser point for the second cycle should be 95 MPa. Therefore, the PPPGS identified this specimen's Kaiser point for the second cycle more accurately

than the tangent-intersection method. Upon observation, we noted that in most of the classification results for the test set, the Kaiser points identified by the PPPGS tended to be more accurate than those identified by the tangent-intersection method. This improvement can be attributed to the robust training of the GA-SVM model, which likely minimized the influence of subjective elements introduced by manual calibration and mitigated the effects of partial noise.

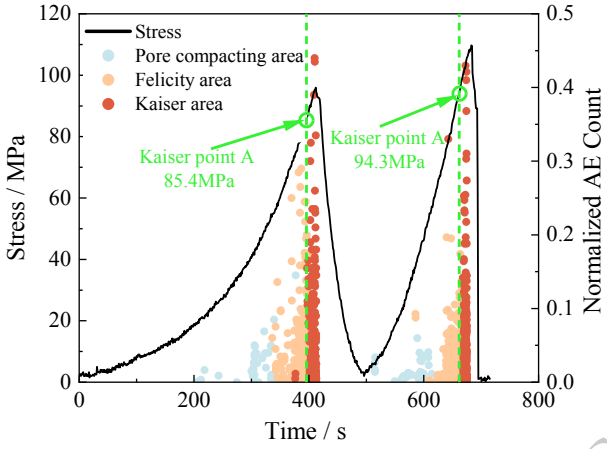

Fig. 14. partitioning results and Kaiser point identification for Specimen 1400-45-3.

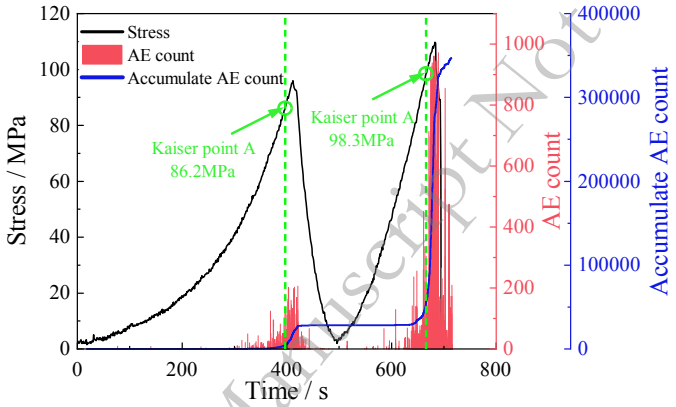

Fig. 15. Identifying Kaiser point in specimen 1400-45-3 using the tangent-intersection method.

4.4 Feature Importance Analysis

To assess the robustness and stability of the model, Permutation Feature Importance (PFI) was employed to conduct feature importance analysis. If the importance score of a particular feature varies significantly across multiple runs, it is considered that the model's dependency on that feature is not sufficiently stable. PFI can also aid in evaluating the importance of each feature for the model's classification capability. It ranks the contribution of each feature to the model, providing directions for model optimization in subsequent research. Fig. 16 shows the average feature importance scores of the model after conducting 20 PFI analyses.

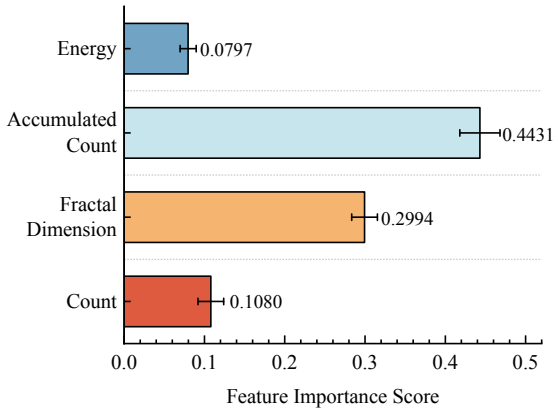

Fig. 16. The Average feature importance scores after 20 PFI analyses.

According to Fig. 16, in the average scores of feature importance, accumulated counts > fractal dimension > energy > count. It can be observed that in the classification of the three regions, the accumulated counts, commonly used in many studies, remain the most critical factor influencing classification. The importance score of the fractal dimension was second only to the accumulated counts, indicating the significant role of the fractal dimension in classifying the three regions and highlighting it as a reliable feature for identifying the Kaiser point. Moreover, the average feature importance scores and relative errors for each feature obtained after performing 20 PFI analyses showed that the errors for each feature were relatively low, indicating that the PSR-GA-SVM model had good robustness and stability.

4.5 The engineering application

A phosphate mine in Weng'an, Guizhou is an underground mine with an annual production of nearly 1.5 million tons. The mining depth of this phosphate mine will reach 1000 m, necessitating effective management of in-situ stress associated with deep mining. Therefore, obtaining accurate in-situ stress information is of paramount importance. This study extracted non-oriented core samples from the mining area and subsequently reoriented them using the non-oriented core ground re-orientation technique [42]. Fig. 17 displays the core extraction site of the Weng'an phosphate mine. Due to the fact that the ore body in this mine has a dip angle of approximately 9°, which is nearly parallel to the horizontal plane, the four-direction method was used to determine the direction of the maximum principal stress to simplify the calculations. The specific solution formula can be found in Eq.(4.5) [43].

$$\left.\begin{matrix}\sigma_H \\ \sigma_h\end{matrix}\right\} = \frac{\sigma_{0^\circ}+\sigma_{90^\circ}}{2} + \frac{\sigma_{0^\circ}-\sigma_{90^\circ}}{2}\cos 2\beta - \frac{\sigma_{0^\circ}-2\sigma_{45^\circ}+\sigma_{90^\circ}}{2}\sin 2\beta \tag{4.5}$$

where σ_H is the maximum horizontal principal stress, σ_h is the minimum horizontal principal stress, and β is the angle between the azimuth of the maximum horizontal principal stress and 0°.

This study selected borehole NZK204 for in-situ stress measurement calculations. After extracting core samples at various depths from the boreholes, the samples were processed into small specimens with a diameter of 25 mm and a height-to-diameter ratio of 2:1. Experimental tests were conducted using the MTS815 servo material testing machine and the PCI-II multi-channel AE system to obtain the AE features of the samples.

Fig. 17. The core extraction site of the Weng'an phosphate mine.

Utilizing the PPPGS, the estimation of in-situ stress information for the Weng'an phosphate mine was conducted, as presented in Table 5. Subsequently, the spatial stress components of the rock mass at different depths were computed based on the information in Table 5, as shown in Table 6. Simultaneously, employing the linear regression method, the measured in-situ stresses at various depths were fitted to generate the curves depicting the variation of in-situ stress with depth for the Weng'an phosphate mine, as illustrated in Figure 18.

Table 5. The in-situ information estimated using the PPPGS.

Core depth/m	Core number	Average stress value/MPa
-500	NZK204-500-0	16.93
	NZK204-500-45	10.21
	NZK204-500-90	13.07
	NZK204-500-V	13.84
-870	NZK204-850-0	21.02
	NZK204-850-45	13.45
	NZK204-850-90	16.53
	NZK204-850-V	19.85
-1025	NZK204-1000-0	24.11
	NZK204-1000-45	17.33
	NZK204-1000-90	23.50
	NZK204-1000-V	27.62

Table 6. Spatial stress components of rock mass at various depths

Core number	Measuring point depth/m	Vertical principal stress /MPa	Maximum horizontal principal stress/MPa	Minimum horizontal principal stress/MPa	Direction of maximum principal stress
NZK204	-500	13.84	20.16	9.83	N35.67°W
	-870	19.85	24.55	13	N36.43°W
	-1025	27.62	30.29	17.32	N41.54°W

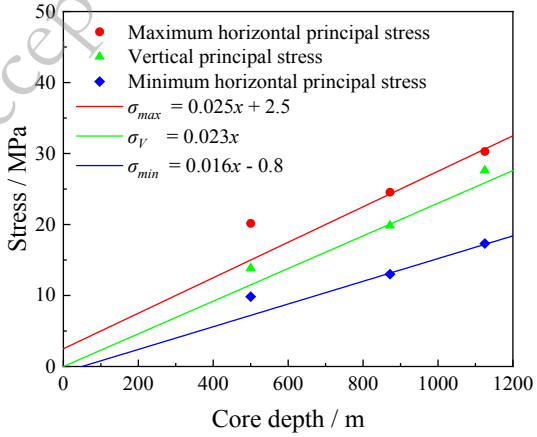

Fig. 18. Curves depicting the variation of in-situ stress with core depth.

Table 7 presents the in-situ stress data obtained at different depths through hydrofracturing method in the mining exploration information. A comparison was made between the method

employed in this study and the hydrofracturing method, revealing that the in-situ stress magnitudes measured by both approaches were very close, with the stress directions differing by no more than 15°. The results obtained by the two methods were relatively consistent. Therefore, the intelligent identification research on Kaiser point conducted in this study provides a viable solution for in-situ stress measurements in mining, and exhibited good performance. By applying the findings of this study to the AE Kaiser effect method, the human and material resources input will be reduced, and the efficiency and accuracy of in-situ stress measurements will be enhanced.

Table 7. Spatial stress components of rock mass at various depths (by hydrofracturing method)

Core number	Measuring point depth/m	Vertical principal stress /MPa	Maximum horizontal principal stress/MPa	Minimum horizontal principal stress/MPa	Direction of maximum principal stress
NZK204	-557	14.76	20.42	12.86	N51°W
	-884	23.43	23.42	16.85	N50°W
	-1031	27.32	29.44	19.58	N55°W

5 Conclusion

To achieve rapid and accurate identification of Kaiser points, this study combines chaos theory with machine learning algorithms to establish an intelligent identification model for Kaiser points. Firstly, AE activities of rock samples were analyzed through PSR to extract the fractal dimension of AE counts. Subsequently, the fractal dimension of AE counts was combined with AE characteristics to construct an AE partitioning intelligent identification model using GA and SVM. Finally, Kaiser points were identified based on the classification results of this model.The conclusions were summarized as follows:

(1) In this study, a dataset comprising AE counts from 60 rock specimens was established. The SVM was utilized to develop the intelligent model for AE count partitioning classification. To construct the model effectively and improve its performance, GA was introduced to optimize the SVM hyperparameters, and SMOTETomek was used to process the unbalanced dataset.

(2) The SVM model was trained using the training set, while the test set was employed to evaluate the performance of the model. The model's accuracy, precision, recall, and F_1 in the test set were at high levels, and the AUC for all three classifications was greater than 0.95. Thus, the model had excellent classification performance.

(3) The identification results of Kaiser point by the PPPGS were very close to those of the tangent-intersection method, indicating that the PPPGS had excellent accuracy in identifying Kaiser point. Notably, the accuracy of the Kaiser point identified through the PPPGS surpassed that identified by the tangent-intersection method.

(4) Upon comparing the average scores of each feature, it was evident that accumulated counts > fractal dimension > energy > count. The score for the fractal dimension was second only to the accumulated counts, signifying the crucial role played by the fractal dimension in classification and underscoring its significance as a reliable feature for identifying Kaiser point.

(5) The PPPGS were applied to measure the in-situ stress of a Weng'an phosphate mine, and exhibited good performance. By applying the findings of this study to the AE Kaiser effect method, the human and material resources input will be reduced, and the efficiency and accuracy of in-situ stress measurements will be enhanced.

Acknowledgments

The authors are grateful for the financial supports from the National Natural Science Foundation of China(Nos. 52374107, 51927808).

Conflict of Interest

The authors declare that they have no conflict of interest.

References

[1] Y. Zhang, H. Qi, C. Li and J. Zhou, Enhancing safety, sustainability, and economics in mining through innovative pillar design:a state-of-the-art review, *J. Saf. Sustain.* (2023).

[2] P. Li, Q.F. Guo, M.F. Cai and S.J. Miao, Present-day state of tectonic stress and tectonization in coastal gold mine area near Laizhou Gulf, North China, *Trans. Nonferrous Met. Soc. China*, 33(2023), No.3, p.865.

[3] Z.Q. Luo, W. Wang, Y.G. Qin and J. Xiang, Early warning of rock mass instability based on multi-field coupling analysis and microseismic monitoring, *Trans. Nonferrous Met. Soc. China*, 29(2019), No.6, p.1285.

[4] N. Tan, R. Yang and Z. Tan, Influence of complicated faults on the differentiation and accumulation of in-situ stress in deep rock mass, *Int. J. Miner. Metall. Mater.*, 30(2023), No.5, p.791.

[5] P. Li and M.F. Cai, Challenges and new insights for exploitation of deep underground metal mineral resources, *Trans. Nonferrous Met. Soc. Chin.*, 31(2021), No.11, p.3478.

[6] P. Li, Q.F. Guo, M.F. Cai and S.J. Miao, Present-day state of tectonic stress and tectonization in coastal gold mine area near Laizhou Gulf, North China, *Trans. Nonferrous Met. Soc. Chin.*, 33(2023), No.3, p.865.

[7] T. Wang, W.W. Ye, L.Y. Liu, K. Liu, N.S. Jiang and X.H. Feng, Disturbance failure mechanism of highly stressed rock in deep excavation: Current status and prospects, *Int. J. Miner. Metall. Mater.*, 31(2024), No.4, p.611.

[8] P. Li, M. Cai, M. Gorjian, F. Ren, X. Xi and P. Wang, Interaction between in situ stress states and tectonic faults: A comment, *Int. J. Miner. Metall. Mater.*, 30(2023), No.7, p.1227.

[9] P. Li, M.F. Cai, Q.F. Guo and S.J. Miao, Characteristics and implications of stress state in a gold mine in Ludong area, China, *Int. J. Miner. Metall. Mater.*, 25(2019), No.12, p.1363.

[10] K. Du, X.B. Li, D.Y. Li and L. Weng, Failure properties of rocks in true triaxial unloading compressive test, *Trans. Nonferrous Met. Soc. Chin.*, 25(2015), No.2, p.571.

[11] K. Li, Y.Y. Wang and X.C. Huang, DDM regression analysis of the in-situ stress field in a non-linear fault zone, *Int. J. Miner. Metall. Mater.*, 19(2012), No.7, p.567.

[12] A. Lavrov, The Kaiser effect in rocks: principles and stress estimation techniques, *Int. J. Rock Mech. Min. Sci.*, 40(2003), No.2, p.151.

[13] J. Kaiser, *Untersuchung über das Auftreten von Geräuschen beim Zugversuch. Dr.-ing* [Dissertation], Fakultät für Maschinenwesen und Elektrotechnik der Technischen …, 1950.

[14] R. E. Goodman, Subaudible noise during compression of rocks, *Geol. Soc. Am. Bull.* 74(1963), No.4, p.487.

[15] G. Boyce, R. Koerner and W. McCabe, *Acoustic emission signatures of various rock types in unconfined compression*, ASTM International West Conshohocken, PA, USA, 1981.

[16] M. Hayashi, T. Kanagawa, S. Hibino, M. Motozima and Y. Kitahara, Detection of anisotropic geo-stresses trying by acoustic emission, and non-linear rock mechanics on large excavating caverns, [in] *Proc. 4th Cong. Int. Soc. for Rock Mechanics*, 1979, p.212.

[17] S.Q. Qin, S.J. Wang, H. Long and J. Liu, A new approach to estimating geo-stresses from laboratory Kaiser effect measurements, *Int J Rock Mech Min Sci*, 36(1999), No.8, p.1073.

[18] E. Villaescusa, M. Seto and G. Baird, Stress measurements from oriented core, *Int. J. Rock Mech. Min. Sci.*, 39(2002), No.5, p.603.

[19] S. Yoshikawa and K. Mogi, A new method for estimation of the crustal stress from cored rock samples: Laboratory study in the case of uniaxial compression, *Tectonophysics*, 74(1981), No.3, p.323.

[20] V. Srinivasan, T. Gupta, T. A. Ansari and T. N. Singh, An experimental study on rock damage and its influence in rock stress memory in a metamorphic rock, *Bull. Eng. Geol. Environ.*, 79(2020), No.8, p.4335.

[21] X. Bai, D. M. Zhang, H. Wang, S. J. Li and Z. Rao, A novel in situ stress measurement method based on acoustic

emission Kaiser effect: a theoretical and experimental study, *Roy. Soc. Open. Sci.*, 5(2018), No.10, p.181263.

[22] X.B. Li and Z.X. Liu, Research on chaos and intelligent identification of acoustic emission in rock mass, *Chin. J. Rock Mech. Eng.*, 24(2005), No.8, p.1296.

[23] J.C. Xue, X.b. Li and Z.x. Liu, Deformation laws of rock mass and safe alarm system of mine slope based on chaotic theory, *J. Cent. South Univ.(Sci. Technol.)*, 44(2013), No.6, p.2476.

[24] Y.J. Cao, J.D. Wang, W. Liu and Y.R. Yang, Wall sheeting diagnosis in fluidized beds based on chaos analysis of acoustic emission signals, *J. Zhejiang Univ.-Sci. a*, 10(2009), No.9, p.1341.

[25] K. Zhao, D.Q. Yan, C.H. Zhong, X.Y. Zhi, X.J. Wang and X.Q. Xiong, Comprehensive analysis method and experimental vertification for in-situstress measurement by acoustic emission tests, *Chin. J. Geotech. Eng.*, 34(2012), No.8, p.1403.

[26] G.F. Wang, Y.X. Zhang and K. Zhao, Research on identification characteristics of Kaiser signal of sandstone, *Rock Soil Mech.*, 31(2010), No.6, p.1913

[27] B. Sivakumar, A. Jayawardena and T. Fernando, River flow forecasting: use of phase-space reconstruction and artificial neural networks approaches, *J. Hydrol.*, 265(2002), No.1, p.225.

[28] S.W. Fei, Fault Diagnosis of Bearing Based on Wavelet Packet Transform-Phase Space Reconstruction-Singular Value Decomposition and SVM Classifier, *Arab. J. Sci. Eng.*, 42(2017), No.5, p.1967.

[29] H. Su, X. Li, B. Yang and Z. Wen, Wavelet support vector machine-based prediction model of dam deformation, *Mech. Syst. Sig. Process.*, 110(2018), p.412.

[30] F. Takens, Detecting strange attractors in turbulence, [in] *In D. Rand, & L. S. Young (Eds.), Dynamical systems and turbulence, Warwick 1980*, 2006, p.366.

[31] P. Grassberger and I. Procaccia, Characterization of Strange Attractors, *Phys. Rev. Lett.*, 50(1983), No.5, p.346.

[32] M. B. Kennel, R. Brown and H. D. I. Abarbanel, Determining embedding dimension for phase-space reconstruction using a geometrical construction, *Phys. Rev. A*, 45(1992), No.6, p.3403.

[33] L. Cao, Practical method for determining the minimum embedding dimension of a scalar time series, *Physica D*, 110(1997), No.1, p.43.

[34] A. M. Fraser and H. L. Swinney, Independent coordinates for strange attractors from mutual information, *Phys. Rev. A*, 33(1986), No.2, p.1134.

[35] R. Wang, J. Gao, Z. Gao, X. Gao, H. Jiang and L. Cui, Data Fusion Based Phase Space Reconstruction from Multi-Time Series, *Int. J. Database Theory Appl.*, 8(2015), No.6, p.101.

[36] M. T. Rosenstein, J. J. Collins and C. J. De Luca, A practical method for calculating largest Lyapunov exponents from small data sets, *Physica D*, 65(1993), No. 1, p.117.

[37] A. Wolf, J. B. Swift, H. L. Swinney and J. A. Vastano, Determining Lyapunov exponents from a time series, *Physica D*, 16(1985), No.3, p.285.

[38] X.Q. Wang, H.K. Ge, L.L. Song, T.M. He and W. Xin, Experimental study of two types of rock sample acoustic emission events and Kaiser effect point recognition approach, *Chin. J. Rock Mech. Eng.*, 30(2011), No.3, p.580.

[39] Q.B. Meng, M.W. Zhang, L.J. Han, H. Pu and Y.L. Chen, Acoustic Emission Characteristics of Red Sandstone Specimens Under Uniaxial Cyclic Loading and Unloading Compression, *Rock Mech. Rock Eng.*, 51(2018), No.4, p.969.

[40] D.Y. Li, Z.D. Liu, P. Xiao, J. Zhou and D. Jahed Armaghani, Intelligent rockburst prediction model with sample category balance using feedforward neural network and Bayesian optimization, *Undergr. Space*, 7(2022), No.5, p.833.

[41] G. E. A. P. A. Batista, R. C. Prati and M. C. Monard, A study of the behavior of several methods for balancing machine learning training data, *ACM SIGKDD Explor. Newsl.*, 6(2004), No.1, p. 20.

[42] X.B. Li, J.Z. Chen, C.D. Ma, L.Q. Huang, C.J. Li, J. Zhang and Y.Z. Zhao, A novel in-situ stress measurement

method incorporating non-oriented core ground re-orientation and acoustic emission: A case study of a deep borehole, *Int. J. Rock Mech. Min. Sci.*, 152(2022), p.105079.

[43] C.D. Ma, G.S. Tan, X.B. Li, J.Q. Xu and J.Z. Chen, Core Orientation Technology Based on Drilling Trajectory Projection and Its Application in In Situ Stress Measurement of the Deepest Shaft in China, *Minerals*, 12(2022), No.5, p.521.